NANO LETTERS

Letter

Cite This: Nano Lett. 2018, 18, 717−724

pubs.acs.org/NanoLett

Periodic Giant Polarization Gradients in Doped $BiFeO_3$ Thin Films

Marco Campanini,*[,†] Rolf Erni,[†] Chan−Ho Yang,[‡] Ramamoorthy Ramesh,[§] and Marta D. Rossell[†]

[†]Electron Microscopy Center, Empa, Überlandstrasse 129, Dübendorf 8600, Switzerland

[‡]Department of Physics, KAIST, Daejeon 305-701, Republic of Korea

[§]Materials Sciences Division, Lawrence Berkeley National Laboratory, Berkeley, California 94720, United States

Supporting Information

ABSTRACT: The ultimate challenge for the development of new multiferroics with enhanced properties lies in achieving nanoscale control of the coupling between different ordering parameters. In oxide-based multiferroics, substitutional cation dopants offer the unparalleled possibility to modify both the electric and magnetic properties at a local scale. Herein it is demonstrated the formation of a dopant-controlled polar pattern in $BiFeO_3$ leading to the spontaneous instauration of periodic polarization waves. In particular, nonpolar Ca-doped rich regions act as spacers between consecutive dopant-depleted regions displaying coupled ferroelectric states. This alternation of layers with different ferroelectric state creates a novel vertical polar structure exhibiting giant polarization gradients as large as 70 $\mu C\ cm^{-2}$ across 30 Å thick domains. The drastic change in the polar state of the film is visualized using high-resolution differential phase-contrast imaging able to map changes in ferroelectric polarization at atomic scale. Furthermore, a periodic distortion in the Fe—O—Fe bonding angle suggests a local variation in the magnetic ordering. The findings provide a new insight into the role of doping and reveal hitherto unexplored means to tailor the functional properties of multiferroics by doping engineering.

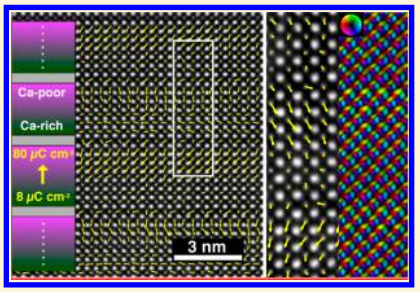

KEYWORDS: *Bismuth ferrite, ferroelectric polarization, doping, scanning transmission electron microscopy, differential-phase contrast*

Multiferroics are intriguing materials with coupled order parameters that permit the control of material properties by different applied stimuli. For instance, in magnetoelectric multiferroics an electrical stimulus results in a magnetic response.[1−5] Such multiferroics rarely occur in nature and thus need to be engineered by, for example, inducing a defined strain state which leads to the desired ferroic coupling essential for technological applications.[6] Local structural instabilities represent degrees of freedom exploitable for the introduction of a specific ferroic ordering or modification of the ones naturally existing, opening unrivaled possibilities to tailor the materials' properties for a wide range of applications that span from spintronics to magnetoelectronics.[7−9] Additionally, the high versatility of the perovskite structure in ferroelectric oxides is a unique playground for the introduction of substitutional species that can alter the electronic properties and magnetism.[10−12] Although the effect of structural distortions on the materials' properties has been widely investigated,[13−17] an atomic scale correlation between substitutional doping and local structural instabilities has not yet been fully addressed. In this framework, achieving a complete understanding of doping effects is of crucial importance for tailoring new materials with enhanced properties.

Bismuth ferrite (BFO) has been widely investigated for being one among the few multiferroic materials that exhibits ferroelectricity and antiferromagnetism at room temperature (RT).[18] In the rhombohedral phase (space group *R*3*c*) BFO is ferroelectric with a large polarization (80−100 $\mu C\ cm^{-2}$) along the [111] direction of the perovskite cell.[19−21] Ferroelectricity of BFO arises from the localized character of the $6s^2$ electrons of the Bi ions that are spatially confined forming a localized lobe (lone-pair) on the A-sites of the perovskite structure.[22] This lone-pair is responsible for the cooperative displacement of the Fe cations and the surrounding O cages along the [111] direction.

Among the different possible dopants, Ca as an A-site dopant is very promising not only for enhancing the magnetoelectric coupling[23] but also for making accessible in BFO thin films novel conducting states and properties, for example, field-controlled conductivity modulation,[24] and electrochromism.[25] In $Bi_{1-x}Ca_xFeO_{3-\delta}$ (δ = x/2) the hole-doping resulting from replacing Bi^{3+} with Ca^{2+} leads to the formation of O vacancies that are organized in self-assembled superstructures,[24−30] which are responsible for the aforementioned effects.

Here we report an atomic resolution investigation of a $Bi_{0.8}Ca_{0.2}FeO_{3-\delta}$ thin film exhibiting periodic dopant fluctuations. We perform a complete analysis of the structural distortions related to the polar instability, discussing the local effect of the substitutional dopants on both ferroelectric and magnetic properties. Our results demonstrate that controlled doping represents an effective tool that can be employed, eventually in combination with strain or other structural distortions, to tailor the material properties at the nanoscale.

Received: September 6, 2017
Revised: December 7, 2017
Published: January 9, 2018

DOI: 10.1021/acs.nanolett.7b03817
Nano Lett. 2018, 18, 717−724

The atomic scale properties of a 85 nm $Bi_{0.8}Ca_{0.2}FeO_{3-\delta}$ film epitaxially grown on $SrTiO_3$ (STO) were investigated by high-resolution scanning transmission electron microscopy (STEM) by means of high-angle annular dark-field (HAADF), annular bright-field (ABF), and differential phase-contrast (DPC). While HAADF-STEM imaging provides a *Z*-contrast signal, particularly sensitive to columns of high atomic number (*Z*), ABF-STEM provides a mean to locate light atomic columns, like oxygen columns. On the other hand, and as explained later in the text, DPC-STEM is a novel technique able to map the local electrostatic field[31] with a great potential impact on ferroelectric materials investigation.

Figure 1a shows an unprocessed HAADF-STEM image of the film in the [010] projection. Herein all the indices are given within the pseudocubic setting of the perovskite structure. The growth direction is from bottom to top (along [001]) and the area corresponds to about one-ninth of the original micrograph rotated by 45° (Figure S1, Supporting Information).

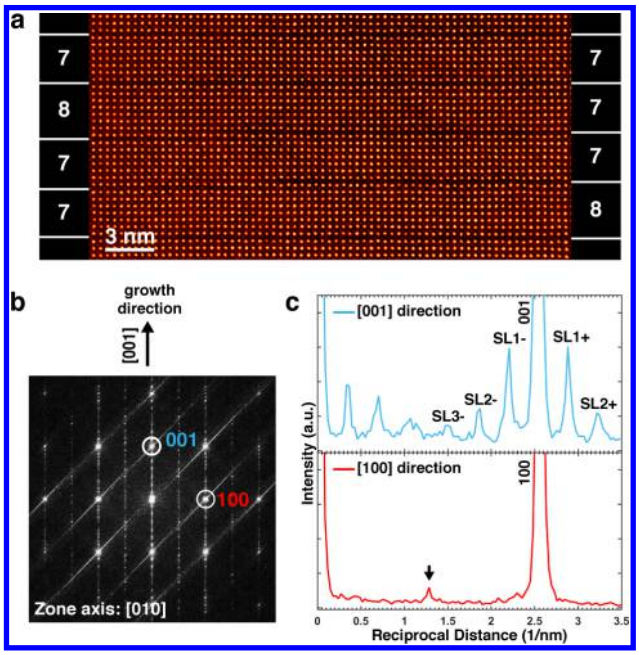

Figure 1. (a) Color-coded HAADF micrograph in the [010] zone axis. The growth direction is from bottom to top. The horizontal white lines indicate the position of the dark-layers at each side of the image, appearing every 7 or 8 perovskite blocks. (b) Corresponding FFT indexed within the pseudocubic reference system. (c) Line profiles along the [001] and [100] directions of the FFT. The satellite spots (SL) due to the superstructure are visible along the [001] direction at a spacing of ~0.35 nm^{-1}, while an additional spot at ~1.28 nm^{-1} (marked by the black arrow) corresponding to a doubling of the perovskite periodicity is observed in the profile taken along the [100] direction.

The film is characterized by the repetition of single planar dark-layers appearing periodically every 7 or 8 perovskite blocks along the growth direction. The lateral extension of these dark-layers is frequently interrupted and a 7-layer perovskite-block band may be transformed into an 8-layer perovskite-block band, and vice versa. The transformation between 7- to 8-layer blocks occurs over steps ~2−3 unit cells wide. These dark-layers have been described in literature as self-assembled structures due to the local accumulation of O vacancies.[29] The fast Fourier transform (FFT) of the full high-resolution image is given in Figure 1b. The line profile in Figure 1c (top) reveals the occurrence of an incommensurate modulation along [001]. In fact, the dark-layers recurring with two different periodicities along the *c*-axis generate incommensurate superlattice reflections (labeled SL in Figure 1c) at a reciprocal distance of ~0.35 nm^{-1}. In real space, the average thickness of the bands separated by the dark-layers is ~7.3 perovskite blocks, in good agreement with the HAADF micrograph shown in Figure 1a. Besides, the line profile along the [010] direction in Figure 1c (bottom) displays a peak (marked by the black arrow) at a reciprocal distance of ~1.28 nm^{-1} corresponding to a real space distance of ~0.78 nm. The periodicity of the perovskite structure (~0.39 nm) along [100] is thus broken resulting in a doubling in this direction. In the following, the origin of the structural features along the a and c directions will be elucidated.

Geometrical phase analysis[32] (GPA) carried out on the full thickness of the film demonstrates that the film is adapted to the STO substrate, whereas a significant out-of-plane dilation (ε_{yy} ~ 4%) is observed only for the dark perovskite layers (Figure S2, Supporting Information). A more detailed quantitative analysis of the lattice distortions was performed by means of peak-pair analysis[33] (PPA), fitting the peaks corresponding to the atomic columns in high-resolution HAADF/ABF-STEM images (see Material and Methods for details). In Figure 2, the PPA analysis on the simultaneously acquired HAADF and ABF-STEM signals along the [010] zone axis is presented. Two dark-layers (marked by the black arrows) are visible in the field of view of the HAADF image (Figure 2a). Following the nomenclature given in the scheme, we analyze the structural distortions by measuring the distance between the peaks corresponding to the atomic columns of the A and B sublattices. In particular, we call $a_{A\text{-}A}$ and $c_{A\text{-}A}$ the interatomic distances of the A-sublattice parallel respectively to [100] and [001], whereas a_{B-B} and c_{B-B} are the analogous distances for the B-sublattice. In Figure 2b, the maps of the interatomic distances are reported. Because of the off-centering of the A and B sublattices, the maps of a_{B-B} and c_{B-B} correspond to the regions marked by the white dashed boxes in the a_{A-A} and c_{A-A} maps. The positions of the dark-layers are marked in each map by the black arrows. No evident in-plane strain is visible for the A-sublattice, while an out-of-plane elongation of the A−A interatomic distances is detected in proximity of the defective layers, in agreement with the GPA analysis. Remarkably, this distortion is not uniform along the entire layer but has a precise pattern in which one A−A pair undergoing a stronger out-of-plane elongation is immediately followed by one A−A pair in which a less pronounced distortion is observed. An opposite trend is instead observed for the B-sublattice. In fact, while no distortion of the B−B interatomic distances is found along the out-of-plane direction, alternated compressive/tensile distortions of the in-plane interatomic distances are detected along the dark-layers. A strong tetragonal distortion ($c_{A\text{-}A}/a_{A\text{-}A}$ ~ 1.07) is observed just at the dark-layers, as proven by the line-profile along [001] shown in Figure 2c. The large standard deviation of the value measured in the dark layers is due to the alternation of A−A pairs with different out-of-plane dilation, previously described. Taking into account the sublattices offset, in the dark-layers the overall distortion occurs in such a way that the stronger out-of-plane elongation of the A−A pair corresponds to the in-plane compression of the B−B distance, followed by a less pronounced out-of-plane A−A elongation in proximity of the in-plane dilated B−B pair. A sketch of the

DOI: 10.1021/acs.nanolett.7b03817
Nano Lett. 2018, 18, 717−724

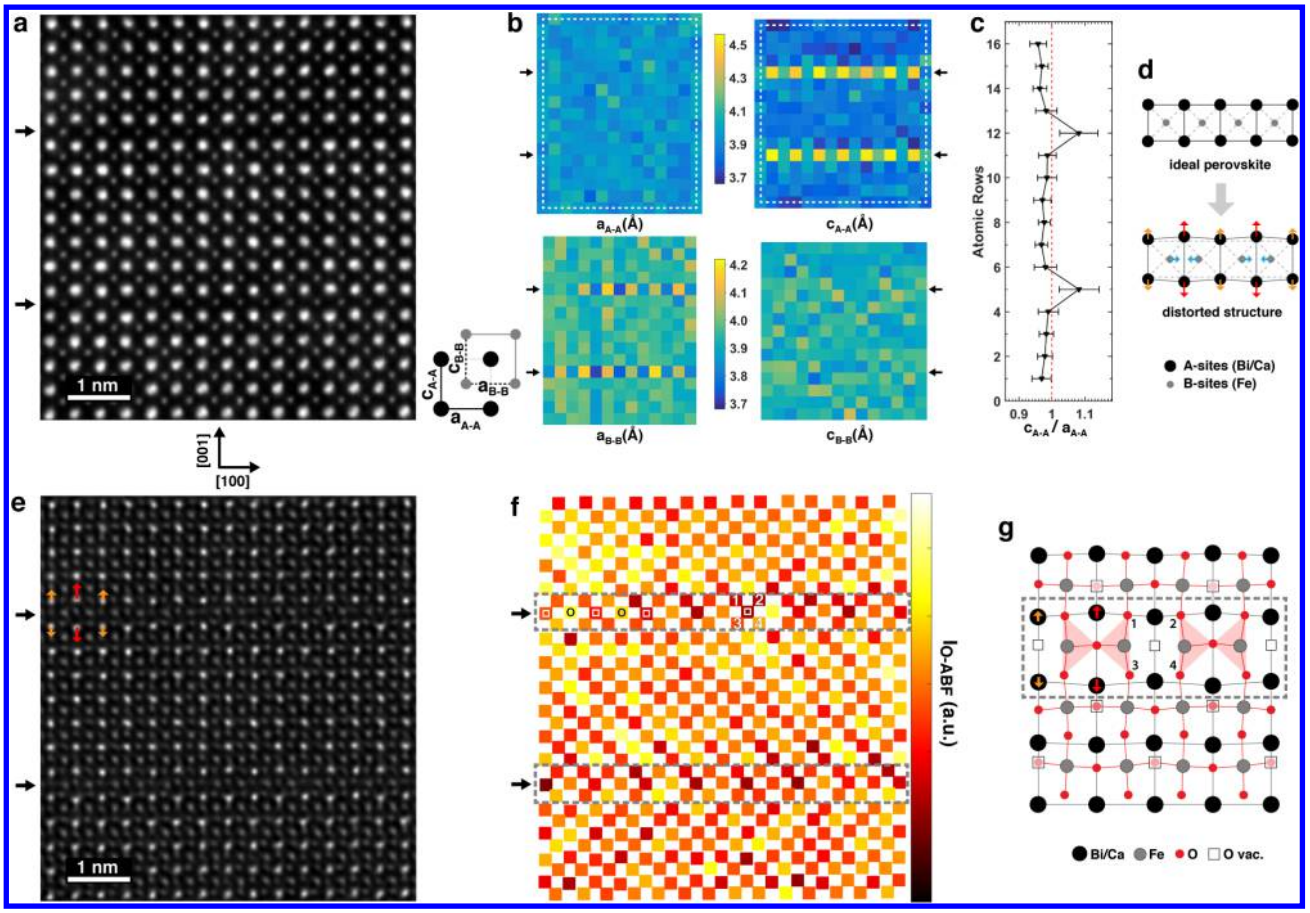

Figure 2. (a) High-resolution HAADF image showing two dark-layers separated by 7-perovskite layers. (b) Maps of the interatomic distances for the A and B sublattices as obtained by PPA. The scheme defines the nomenclature for the two sublattices. (c) Profile along [001] of the tetragonal distortion. (d) Schematic representation (not in scale) of the structural distortions occurring in the dark-layers. (e) Corresponding inverted-ABF image. (f) Fit of the intensities of the O atomic columns plotted at their fitted coordinates. A chessboard-like pattern of O intensities is visible, because the effect is stronger in the region immediately following the dark-layers along the [001] direction. (g) Schematic representation of the O vacancies ordering into the distorted cations lattice. The portion of the model in the gray dashed box corresponds to a dark-layer, where O vacancies are preferentially organized. The partial O vacancies ordering in the other layers is depicted by semitransparent white boxes.

distorted structure is shown in Figure 2d. The doubling of the periodicity along [100] generated by this structural distortion is responsible for the diffraction peak at ∼1.28 nm^{-1} mentioned above.

The simultaneously acquired ABF-STEM signal is shown in Figure 2e, after inverting the contrast (see Materials and Methods for details). The two layers that appeared as dark-layers in HAADF-STEM exhibit here a lower total intensity in the inverted signal. In Figure 2f, the intensity of all the O atomic columns is plotted at the fitted atomic positions. Taking the profiles along the directions indicated by the arrows, we observe an ordering of O vacancies appearing as an alternation of more intense O atomic columns (labeled as O) and less intense O columns (labeled by a white square), in which the O vacancies are preferentially localized. The atomic columns displaying a higher O content are located between the more spaced A−A pairs and the closer B−B pairs, as sketched in Figure 2g. In the defective layers, the Fe cations are thus shifted toward the less deficient O columns resulting in a local reduction of the Fe−O bond length. It is worth noting that (i) beside the preferential ordering in the defective layers a chessboard-like pattern, which can be attributed to a partial ordering of O vacancies, is observed throughout the perovskite blocks at both sides of the dark-layers; (ii) in the defective layers, the O nearest-neighbors of the O vacancy (labeled as 1−4 in Figure 2f ,g) are shifted toward the O vacancy, inducing a tetragonal coordination around the Fe cations. These results are in agreement with the average reduction of the Fe—O bond length recently proposed for polycrystalline $Bi_{0.9}Ca_{0.1}FeO_{3-\delta}$ samples.[34] Our results demonstrate that the ordering of O vacancies and the cations sublattices distortions are strongly coupled and the contraction of the Fe—O bond length is a localized effect.

In order to investigate the distribution of the Ca dopants, we did an analysis of the HAADF/ABF signal intensities taking line profiles along the [001] direction over an area of about 25 nm^2. The profile reported in Figure 3a shows a fluctuation of the HAADF intensity which is periodic and is repeated for each block composing the superstructure. In particular after each dark-layer, whose position is marked by a black arrow and is characterized by a lower integrated intensity (area colored in gray), we observe a linear increase of the HAADF intensity until the next dark-layer. This intensity variation can be attributed to a decrease of the Ca doping within the intermediate perovskite blocks along [001]. These spontaneously generated dopant fluctuations are effective in producing a layering within the structure with Ca-rich and Ca-poor regions. On the contrary, a correlation of the HAADF

DOI: 10.1021/acs.nanolett.7b03817
Nano Lett. 2018, 18, 717−724

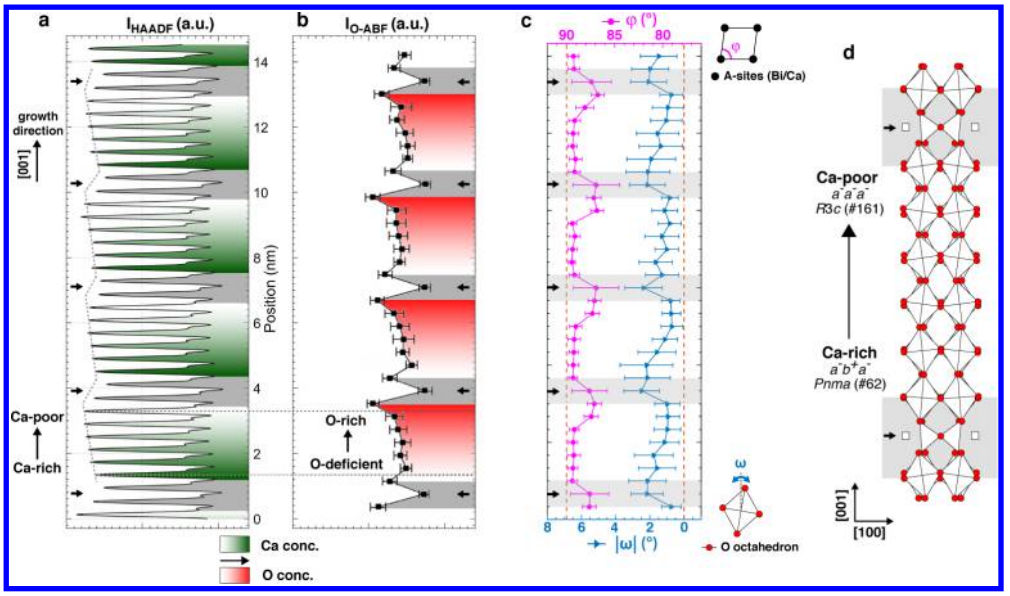

Figure 3. (a) HAADF and (b) inverted-ABF intensity profiles along the [001] direction. Periodic fluctuations of the HAADF intensity are observed for each block composing the superstructure between consecutive dark-layers (marked in gray). A similar trend is visible in the inverted-ABF profile, which can be related to a variation of O concentration. (c) Profiles along [001] of the perovskite cell angle (φ) and O-octahedron tilting amplitude ($|\omega|$). (d) Scheme of the doping-induced distortion of the O-octahedron tilting pattern, showing a structural phase transformation from *Pnma* to *R*3*c* space group as the doping concentration decreases.

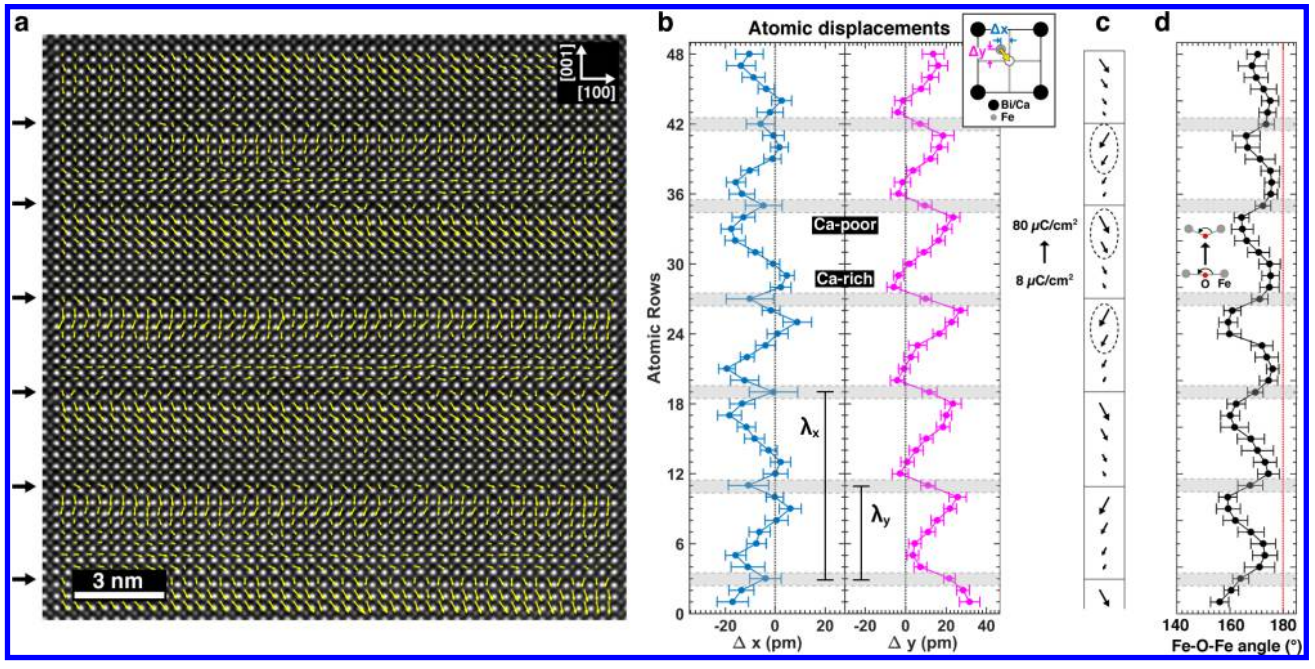

Figure 4. (a) Polarization map superimposed to the HAADF image. The black arrows on the left indicate the position of the dark-layers. (b) Profiles along the [001] direction of the in-plane (Δx) and out-of-plane (Δy) components of the atomic displacements. Scheme of the relationship between atomic displacements and the projected ferroelectric polarization is given in the inset. (c) Sketch of the complex polar structure of the film, showing a periodic polarization wave. Coupled ferroelectric domains exist in the periodic superstructure (dashed circles). (d) Profile along [001] of the Fe—O—Fe bonding angle that highlights a straightening of the superexchange path in the Ca-rich areas with respect to the ferroelectric regions.

signal and Ca concentration in the dark-layers is not possible due to strain effects that locally affect the channeling of the electron beam. Though a quantitative interpretation of the ABF-STEM signal is less straightforward, taking the intensity profile of the fitted O columns located at the FeO_2 layers perpendicular to the growth direction, we observe a similar tendency. The O content increases from the Ca-rich toward the Ca-poor areas (Figure 3b). A deviation from this general trend is observed for the O layers respectively above and below the defective layers which exhibit a local higher O content. This self-induced effect shall compensate for the oxygen (and electron) deficient state in the defective layers, thus preserving the charge neutrality.

In Figure 3c, we report the profiles of structural distortions of the perovskite cells, that is, the angle of the perovskite cell (ϕ) and the O octahedron tilting amplitude ($|\omega|$). Remarkably, a periodic pattern following the dopant profile is observed and an angle $\phi = 89.3 \pm 0.5°$ is observed except for the layers close to

DOI: 10.1021/acs.nanolett.7b03817
Nano Lett. 2018, 18, 717−724

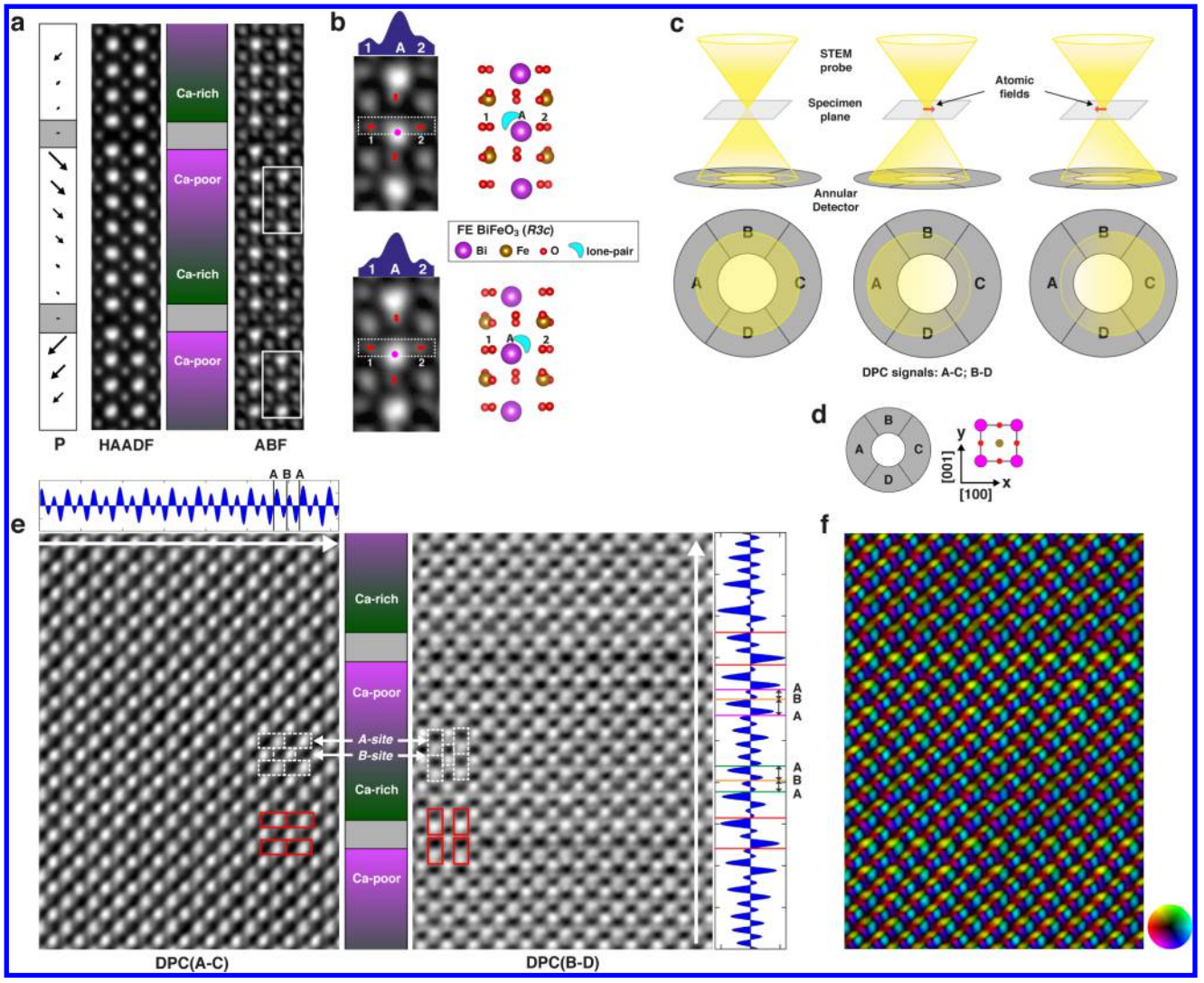

Figure 5. (a) HAADF and ABF motifs (lateral width: 1.1 nm) obtained averaging a template over the field of view of Figure 2a,e, respectively. The corresponding polarization and dopant fluctuations are given in the schemes. The dark-layers are marked by gray boxes. (b) Magnified views of two consecutive Ca-poor regions, corresponding to the areas marked by the white boxes in (a). The atomic configurations of these two regions are horizontally flipped, thus explaining the change of sign of the in-plane component of polarization in two consecutive layers. (c) Schematic representation of the basic principle of the DPC technique. (d) Sketch of the sample orientation with respect to the segmented detector. (e) Differential signals between opposite segments (A−C, B−D) of the detector on an area showing the same structure as in panel a. The line profiles of the two signals are obtained along the directions of the arrows. (f) Vector plot of the atomic electric fields, where the hue gives the field direction and the saturation is proportional to the vector modulus.

the dark-layers, which are affected by the structural distortions. On the other hand, the average O octahedron tilting amplitude decreases along the perovskite block from ∼2° toward zero, consistent with a transition between an in-phase toward an out-of-phase tilting scheme from the Ca-rich toward the Ca-deficient area. This trend in the structural distortions highlights a progressive variation from a higher toward a lower symmetry space group moving from Ca-rich toward Ca-poor areas (Figure 3d), revealing a structure that is doping-controlled at the nanoscale.

The ferroelectric state of the film was studied by analyzing the geometrical displacements of the cations sublattices in high-resolution HAADF-STEM. In BFO, the modulus of the atomic-scale polarization is proportional to the displacement of Fe cation with respect to the center of mass of the Bi cell and its direction is opposite to such displacement.[35] In Figure 4a, a polarization map (see Materials and Methods for details) is plotted superimposed to an HAADF-STEM image taken in the [010] zone axis where six dark-layers are visible. The map shows a periodic alternation of ferroelectric domains and layers in which the ferroelectric instability is quenched, corresponding to Ca-poor and Ca-rich regions, respectively. With respect to different systems characterized by a lateral juxtaposition of polar and nonpolar regions, for example, columnar systems containing a ferroelectric perovskite and a ferromagnetic spinel,[36,37] in the present system the dopant ordering along the growing direction produces alternated ferroelectric/non-ferroelectric regions that are stacked along the direction normal to the film surface, giving rise to a vertical polar superstructure. It is worth noting that the polarization of the ferroelectric domains appears in this projection to be parallel either to the $[10\bar{1}]$ or $[\bar{1}0\bar{1}]$ directions, in agreement with a global polarization vector along [111] as typically observed for undoped BFO. A further confirmation regarding the displace-

DOI: 10.1021/acs.nanolett.7b03817
Nano Lett. 2018, 18, 717−724

ments geometry is obtained analyzing the film polarization along a different projection, for example, [110] zone axis (see Figure S3, Supporting Information). Ferroelectric domains arising due to an inversion in the doping ordering, that is, with Ca-content increasing in the intermediate perovskite blocks along the film growth direction, were also observed in different portions of the TEM sample, in agreement with the macroscopic characterizations of similar films previously reported in refs 24 and 25.

In Figure 4b, the profiles of the atomic displacements at the origin of the ferroelectric properties are shown. The displacements of Fe along the [100] and [001] directions, named respectively Δx and Δy, display different periodicities, being the periodicity of Δx the double of the one of Δy ($\lambda_x = 2\lambda_y$). The different periodicities in the atomic displacements are correlated to the establishment of symmetric coupled ferroelectric domains in consecutive Ca-depleted regions. A schematic representation of the film polar structure is given in Figure 4c, where the coupled ferroelectric domains are marked by dashed circles. Despite some asymmetries due to small residual mistilt, in the ferroelectric Bi-rich areas an average total displacement of the Fe cations of ∼31 pm was measured. Additionally, the Δx value obtained in the dark-layers confirms that the atomic displacements are affected by the local structural strain: in particular, a small value with a large standard deviation is originated by the alternated positive and negative horizontal displacements of Fe cations, arising from the B−B pairs distortions previously shown in Figure 2g. The Ca-doping fluctuations induce therefore a periodic ferroelectric polarization wave with a polarization vector modulus that goes from a nearly zero value of $P_{min} \approx 8$ μC cm^{-2} in the Ca-rich areas toward a maximum value $P_{max} \approx 80$ μC cm^{-2} in the Ca-poor regions, calculated under the Born effective charge[38] approximation. Such an abrupt change in polarization, effectively about 70 μC cm^{-2} across only 30 Å, results in an unprecedented giant polarization gradient 2 orders of magnitude larger than the one recently reported for compositionally graded $Ba_{1-x}Sr_xTiO_3$ thin films.[39]

Furthermore, the geometrical distortion at the origin of the polar instability has an additional relevant effect. In fact, despite the previously discussed doping-dependent pattern in the tilting scheme of the O octahedrons, the different Fe displacements in the Ca-poor and Ca-rich areas are effective in producing a local variation in the Fe—O—Fe angle, which has a notable relevance for the magnetic properties of the system. The profile of the Fe—O—Fe angle shown in Figure 4d highlights a distortion scheme that resembles the trend of the Ca-doping. In particular, an angle close to 180° that favors an AFM interaction (GKA exchange) is observed in the Ca-rich part, while a severe bond buckling occurs in the Ca-poor areas. In agreement with the results of Chou et al.,[34] a local and periodic modification in the superexchange interaction represents an effective way to break the undesired cycloidal spin modulation,[40] which prevents the instauration of a net magnetic moment in undoped BFO.

An analysis of the lone-pair ordering at the base of the observed ferroelectric structure was carried out by combining HAADF/ABF-STEM imaging and DPC-STEM (Figure 5). In Figure 5a, the statistical averages (see Materials and Methods for details) of a region containing two defective layers are presented for both HAADF and inverted ABF-STEM signals, together with a schematic representation of the corresponding dopant and polarization profiles. The two areas marked by white rectangles belonging to two consecutive Ca-poor regions are reported at a magnified scale in Figure 5b. In these zoomed images, the A-site cations present nonsymmetric coordination geometry. In particular, the vertical off-centering with respect to the surrounding O columns occurs for both regions with an upward displacement of the anions surrounding the cation. On the contrary, displacements with opposite sign are observed along the horizontal direction in consecutive Ca-poor regions, as highlighted by the two line-profiles taken along the white dashed rectangles. This coordination geometry in the Ca-poor regions agrees well with the one of undoped BFO (*R*3*c* space group), as visible by the comparison with the structural models reported as reference in Figure 5b for both analyzed regions. Such asymmetric coordination around the A-site is attributed to a different preferential localization of the lone pair, as depicted in the scheme.

Electric field imaging of single atoms by means of DPC has recently been demonstrated, opening new perspectives in materials investigation at the atomic scale.[41] Here we present an analysis of the atomic electrostatic fields as an experimental proof of the complex polar state occurring in the Ca-doped BFO film. Figure 5c shows a schematic representation of the principle of DPC. In this technique, the origin of the differential signal between opposite pairs of quadrants (A,C and B,D) in the segmented annular dark-field detector is due to the deflection of the beam by local electric fields in the specimen.[31,41] In our investigation, we oriented the sample with the [100] and [001] directions parallel to the A−C and B−D segments of the detector, respectively (Figure 5d).

In Figure 5e, the DPC(A−C) and DPC(B−D) differential signals are shown. Taking a profile over the entire field of view of DPC(A−C) along the direction of the white arrow, an antisymmetric profile is obtained at each zero-crossing corresponding either to A or B sites. On the contrary, taking a similar profile of the DPC(B−D) along the perpendicular direction, some peculiar features emerge. In particular, (i) a strong asymmetry is observed at the zero crossing for the A-sites in the defective layers (indicated by the red lines), (ii) a transition from an antisymmetric toward an asymmetric profile is observed at the zero crossing for the B-site (indicated by the orange lines) moving from the Ca-rich toward the Ca-poor areas, (iii) the position of the zero crossing for the B-site undergoes a vertical shift that resemble the cationic displacements responsible for the establishment of a ferroelectric polarization in the Ca-poor layers of the sample. In Figure 5f, an atomic resolution color map of the atomic fields is reported showing an increase of polarization from the Ca-rich toward the Ca-poor regions visible as an asymmetry in the color pattern. These results prove that DPC is hence a suitable technique to detect atomic electric field fluctuations, paving the way for new insights into ferroelectric materials.

In conclusion, the presented atomic-scale analysis demonstrates that the spontaneous formation of a layered structure of substitutional dopants is effective in creating a complex ferroelectric structure constituted by the alternation of polar and nonpolar domains. This polar pattern showing giant polarization gradients has been investigated combining several advanced scanning transmission electron microscopy techniques at the atomic level, that is, HAADF/ABF and DPC. In particular, periodic fluctuations in the Ca dopant concentration are at the origin of the breaking of the lone-pair ordering scheme, producing a local quenching of the ferroelectricity and a local straightening of the Fe—O—Fe bond angle which is

DOI: 10.1021/acs.nanolett.7b03817
Nano Lett. 2018, 18, 717−724

expected to be advantageous for the magnetic properties. These findings provide a new insight into the role of doping in complex ferroelectric structures in which anisotropic dopants/vacancies distribution can occur and represent a proof of concept that controlled substitutional doping is a powerful tool exploitable to create artificial structures with complex polar patterns and giant polarization gradients, such as polarization waves.

Materials and Methods. *Sample Preparation.* Ca-doped (20%) $BiFeO_3$ films with a thickness of 85 nm were grown on $SrTiO_3$(001) substrate using pulsed laser deposition at 873−923 K in 50−100 mTorr O_2 pressure. Typical deposition rates were about 2 nm min^{-1} with a laser repetition rate of 10 Hz. The pulsed KrF excimer laser (wavelength: 248 nm) was focused to reach a laser fluency of ∼2 J cm^{-2} on the target surface. The films were cooled down at a rate of 5 K min^{-1} with ∼1 atm O_2 pressure.

High-Resolution Scanning Transmission Electron Microscopy. Electron transparent cross-sectioned samples for transmission electron microcopy were prepared by means of a FEI Helios NanoLab 600i and a FEI Helios NanoLab 450S focused ion beam operated at accelerating voltages of 30 and 5 kV. The specimens' thicknesses were in the range 30−60 nm. Plasma-cleaning (25% O_2, 75% Ar) was performed for 60 s on the specimens before STEM experiments. HAADF and simultaneous ABF STEM were performed on an aberration-corrected JEOL ARM200F, operated at 200 kV. The experiments were carried out setting a probe semiconvergence angle of 18 mrad and collecting semiangles of 90−170 mrad for HAADF and 9−18 for ABF. All the ABF images are here presented after inverting the signal, that is, peaks corresponding to atomic columns appear as local intensity maxima in the images.

Differential-Phase Contrast. In DPC techniques, a deflection of the center of mass of the transmitted disk is observed due to the electric fields in the specimen plane. DPC investigation was carried out on an aberration-corrected Titan Themis 80-300 operated at 300 kV with a probe-forming aperture semiangle of 18 mrad and a collection angular range for the segmented DF4 detector set to 9−57 mrad. The orientation of the samples with respect to the detector segments was set as described in the text.

Data Processing and Analysis. HAADF and ABF images of Figures 2 and 3 were obtained as averages of time series of 10 frames, after nonrigid registration using the Smart Align[42] software. HAADF whose signal is proportional to Z^n ($n \approx 1.6-2.0$) was employed to map the Ca doping, thanks to its strong sensitivity to atomic number. On the contrary, ABF signal is proportional to Z^m ($m \approx 1/3$) and can be successfully employed to visualize light elements, like oxygen.[43] Making use of ABF, we investigated the ordering of O vacancies and the structural distortions related to the anionic sublattice.

The picometer-precision fitting of the peaks corresponding to the atomic columns was computed on both HAADF and ABF signals by means of 7 parameters Gaussians, using a custom-developed Matlab code based on the method proposed by Yankovich et al.[44]

Following Bals et al.,[45] in an ideal crystal (i.e., a crystal with constant interatomic distances) the precision of the atomic columns fitting can be defined as the standard deviation (σ) of the lattice separations. We carried out an analogous statistical analysis, calculating the σ of the interatomic distances for Bi, Fe, and O species. Such calculation was performed excluding the layers mostly affected by the strain, that is, the dark-layers and their nearest-neighbors (see Figure 2b,c). The following values were obtained for the different species: σ_{Bi} = 5.8 pm, σ_{Fe} = 3.6 pm, and σ_O = 4.3 pm. Because of the complexity of our system displaying a doping gradient along the entire perovskite block, these values represent an overestimation of the precision of the fitting algorithm. Nevertheless, the reduced precision in the fitting of the Bi columns positions with respect to Fe and O species can be remarkably attributed to an increase of their local static displacements, induced by the substitution of Ca dopant on the A-site of the perovskite structure.

The precise fitting of the peaks in the HAADF/ABF images permits to directly access the projected crystallographic structure and make quantitative analysis, by, for example, PPA. In this way, the structural distortions are immediately accessible by direct imaging of the crystal structure along the selected crystallographic orientation. Distortion analysis and polarization mapping were performed using custom-developed Matlab codes. The atomic column positions were fitted over the entire field-of-view of the time-averaged ABF/HAADF signals; afterward, the profiles along the [001] direction were calculated averaging along the [010] direction the corresponding distortion/displacement maps. The averages represent the estimated values while the standard deviations give the error bars. Atomic-scale polarization maps were calculated by measuring the off-centering between the B-site position and the center of the A-site cell, following the method proposed by Nelson et al.[35]

In order to compare HAADF/ABF signals to DPC we used the approach of template-matching. By means of template-matching, a statistical average of a representative portion of the sample (motif) can be obtained. In particular, the statistically equivalent averaged motifs for both HAADF and ABF signals were determined by cross-correlation and averaging using the MacTempas[46] software package.

■ ASSOCIATED CONTENT

Supporting Information

The Supporting Information is available free of charge on the ACS Publications website at DOI: 10.1021/acs.nanolett.7b03817.

Large-scale morphology of the film superstructure (Figure S1). Description of the strain state of the film by GPA analysis (Figure S2). Polarization analysis along the complementary [110] pseudocubic direction (Figure S3) (PDF)

■ AUTHOR INFORMATION

Corresponding Author

*E-mail: marco.campanini@empa.ch.

ORCID

Marco Campanini: 0000-0003-4312-4794

Author Contributions

C.-H.Y. and R.R. carried out the thin films growth. M.D.R. prepared the electron transparent TEM specimens. M.C. and M.D.R. conducted the HAADF/ABF-STEM experiments. M.C. performed DPC-STEM experiments and the data analysis. M.C. wrote the manuscript supervised by R.E. and M.D.R. M.D.R. coordinated the project. All the authors discussed the results and commented on the manuscript.

Notes

The authors declare no competing financial interest.

DOI: 10.1021/acs.nanolett.7b03817
Nano Lett. 2018, 18, 717−724

■ ACKNOWLEDGMENTS

M.C. thanks NCCR-MARVEL project funded by the Swiss National Science Foundation (SNSF) for the financial support. Access to the TEM facility at the IBM Research-Zürich (Switzerland) under the IBM/Empa Master Joint Development Agreement is gratefully acknowledged. The work at KAIST was supported by the National Research Foundation (NRF) grant funded by the Korean government (NRF-2017R1A3B1023686).

■ REFERENCES

(1) Spaldin, N. A.; Fiebig, M. *Science* **2005**, *309*, 391.
(2) Eerenstein, W.; Mathur, N. D.; Scott, J. F. *Nature* **2006**, *442*, 759.
(3) Cheong, S.-W.; Mostovoy, M. *Nat. Mater.* **2007**, *6*, 13.
(4) Ramesh, R.; Spaldin, N. A. *Nat. Mater.* **2007**, *6*, 21.
(5) Fiebig, M.; Lottermoser, T.; Meier, D.; Trassin, M. *Nat. Rev. Mats.* **2016**, *1*, 16046.
(6) Hill, N. A. *J. Phys. Chem. B* **2000**, *104*, 6694.
(7) Scott, J. F. *Science* **2007**, *315*, 954.
(8) Béa, H.; Gajek, M.; Bibes, M.; Barthélémy, A. *J. Phys.: Condens. Matter* **2008**, *20*, 434221.
(9) Bibes, M.; Barthelemy, A. *Nat. Mater.* **2008**, *7*, 425.
(10) Ahn, C. H.; Triscone, J.-M.; Mannhart, J. *Nature* **2003**, *424*, 1015.
(11) Yang, C.-H.; Kan, D.; Takeuchi, I.; Nagarajan, V.; Seidel, J. *Phys. Chem. Chem. Phys.* **2012**, *14*, 15953.
(12) Park, J.; Kang, M.; Kim, J.; Lee, S.; Jang, K.-H.; Pirogov, A.; Park, J.-G.; Lee, C.; Park, S.-H.; Kim, H. C. *Phys. Rev. B: Condens. Matter Mater. Phys.* **2009**, *79*, 064417.
(13) Choi, K. J.; Biegalski, M.; Li, Y. L.; Sharan, A.; Schubert, J.; Uecker, R.; Reiche, P.; Chen, Y. B.; Pan, X. Q.; Gopalan, V.; Chen, L.-Q.; Schlom, D. G.; Eom, C.-B. *Science* **2004**, *306*, 1005.
(14) Haeni, J. H.; Irvin, P.; Chang, W.; Uecker, R.; Reiche, P.; Li, Y. L.; Choudhury, S.; Tian, W.; Hawley, M. E.; Craigo, B.; Tagantsev, A. K.; Pan, X. Q.; Streiffer, S. K.; Chen, L. Q.; Kirchoefer, S. W.; Levy, J.; Schlom, D. G. *Nature* **2004**, *430*, 758.
(15) Jang, H. W.; Ortiz, D.; Baek, S.-H.; Folkman, C. M.; Das, R. R.; Shafer, P.; Chen, Y.; Nelson, C. T.; Pan, X.; Ramesh, R.; Eom, C.-B. *Adv. Mater.* **2009**, *21*, 817.
(16) Rossell, M. D.; Erni, R.; Prange, M. P.; Idrobo, J.-C.; Luo, W.; Zeches, R. J.; Pantelides, S. T.; Ramesh, R. *Phys. Rev. Lett.* **2012**, *108*, 047601.
(17) Guzmán, R.; Maurel, L.; Langenberg, E.; Lupini, A. R.; Algarabel, P. A.; Pardo, J. A.; Magén, C. *Nano Lett.* **2016**, *16*, 2221.
(18) Catalan, G.; Scott, F. J. *Adv. Mater.* **2009**, *21*, 2463.
(19) Wang, J.; Neaton, J. B.; Zheng, H.; Nagarajan, V.; Ogale, S. B.; Liu, B.; Viehland, D.; Vaithyanathan, V.; Schlom, D. G.; Waghmare, U. V.; Spaldin, N. A.; Rabe, K. M.; Wuttig, M.; Ramesh, R. *Science* **2003**, *299*, 1719.
(20) Yun, K. Y.; Noda, M.; Okuyama, M.; Saeki, H.; Tabata, H.; Saito, K. *J. Appl. Phys.* **2004**, *96*, 3399.
(21) Das, R. R.; Kim, D. M.; Baek, S. H.; Eom, C. B.; Zavaliche, F.; Yang, S. Y.; Ramesh, R.; Chen, Y. B.; Pan, X. Q.; Ke, X.; Rzchowski, M. S.; Streiffer, S. K. *Appl. Phys. Lett.* **2006**, *88*, 242904.
(22) Ravindran, P.; Vidya, R.; Kjekshus, A.; Fjellvåg, H.; Eriksson, O. *Phys. Rev. B: Condens. Matter Mater. Phys.* **2006**, *74*, 224412.
(23) Catalan, G.; Sardar, K.; Church, N. S.; Scott, J. F.; Harrison, R. J.; Redfern, S. A. T. *Phys. Rev. B: Condens. Matter Mater. Phys.* **2009**, *79*, 212415.
(24) Yang, C.-H.; Seidel, J.; Kim, S. Y.; Rossen, P. B.; Yu, P.; Gajek, M.; Chu, Y. H.; Martin, L. W.; Holcomb, M. B.; He, Q.; Maksymovych, P.; Balke, N.; Kalinin, S. V.; Baddorf, A. P.; Basu, S. R.; Scullin, M. L.; Ramesh, R. *Nat. Mater.* **2009**, *8*, 485.
(25) Seidel, J.; Luo, W.; Suresha, S. J.; Nguyen, P.-K.; Lee, A. S.; Kim, S.-Y.; Yang, C.-H.; Pennycook, S. J.; Pantelides, S. T.; Scott, J. F.; Ramesh, R. *Nat. Commun.* **2012**, *3*, 799.
(26) Chen, W.-T.; Williams, A. J.; Ortega-San-Martin, L.; Li, M.; Sinclair, D. C.; Zhou, W.; Attfield, J. P. *Chem. Mater.* **2009**, *21*, 2085.
(27) Lepoittevin, C.; Malo, S.; Barrier, N.; Nguyen, N.; Van Tendeloo, G.; Hervieu, M. *J. Solid State Chem.* **2008**, *181*, 2601.
(28) Schiemer, J.; Withers, R.; Norén, L.; Liu, Y.; Bourgeois, L.; Stewart, G. *Chem. Mater.* **2009**, *21*, 4223.
(29) Jang, H.; Kerr, G.; Lim, J. S.; Yang, C.-H.; Kao, C.-C.; Lee, J.-S. *Sci. Rep.* **2015**, *5*, 12402.
(30) Schiemer, J. A.; Withers, R. L.; Liu, Y.; Carpenter, M. A. *Chem. Mater.* **2013**, *25*, 4436.
(31) Shibata, N.; Findlay, S. D.; Kohno, Y.; Sawada, H.; Kondo, Y.; Ikuhara, Y. *Nat. Phys.* **2012**, *8*, 611.
(32) Hÿtch, M. J.; Snoeck, E.; Kilaas, R. *Ultramicroscopy* **1998**, *74*, 131.
(33) Galindo, P. L.; Kret, S.; Sanchez, A. M.; Laval, J.-Y.; Yáñez, A.; Pizarro, J.; Guerrero, E.; Ben, T.; Molina, S. I. *Ultramicroscopy* **2007**, *107*, 1186.
(34) Chou, H.; Yen, C.-W.; Yang, C.-C.; Dwivedi, G.D.; Yang, K. S.; Wu, C. P.; Liu, K. C.; Li, W.-H. *Acta Mater.* **2016**, *111*, 297.
(35) Nelson, C. T.; Winchester, B.; Zhang, Y.; Kim, S.-J.; Melville, A.; Adamo, C.; Folkman, C. M.; Baek, S.-H.; Eom, C.-B.; Schlom, D. G.; Chen, L.-Q.; Pan, X. *Nano Lett.* **2011**, *11*, 828.
(36) Zhan, Q.; Yu, R.; Crane, S. P.; Zheng, H.; Kisielowski, C.; Ramesh, R. *Appl. Phys. Lett.* **2006**, *89*, 172902.
(37) Liu, H.; Liang, W.; Chu, Y.; Zheng, H.; Ramesh, R. *MRS Commun.* **2014**, *4*, 31.
(38) Neaton, J. B.; Ederer, C.; Waghmare, U. V.; Spaldin, N. A.; Rabe, K. M. *Phys. Rev. B: Condens. Matter Mater. Phys.* **2005**, *71*, 014113.
(39) Damodaran, A. R.; Pandya, S.; Qi, Y.; Hsu, S.-L.; Liu, S.; Nelson, C.; Dasgupta, A.; Ercius, P.; Ophus, C.; Dedon, L. R.; Agar, J. C.; Lu, H.; Zhang, J.; Minor, A. M.; Rappe, A. M.; Martin, L. W. *Nat. Commun.* **2017**, *8*, 14961.
(40) Ederer, C.; Spaldin, N. A. *Phys. Rev. B: Condens. Matter Mater. Phys.* **2005**, *71*, 060401.
(41) Shibata, N.; Seki, T.; Sánchez-Santolino, G.; Findlay, S. D.; Kohno, Y.; Matsumoto, T.; Ishikawa, R.; Ikuhara, Y. *Nat. Commun.* **2017**, *8*, 15631.
(42) Jones, L.; Yang, H.; Pennycook, T. J.; Marshall, M. S. J.; Van Aert, S.; Browning, N. D.; Castell, M. R.; Nellist, P. D. *Adv. Struct. Chem. Imag.* **2015**, *1*, 8.
(43) Findlay, S. D.; Shibata, N.; Sawada, H.; Okunishi, E.; Kondo, Y.; Ikuhara, Y. *Ultramicroscopy* **2010**, *110*, 903.
(44) Yankovich, A. B.; Berkels, B.; Dahmen, W.; Binev, P.; Sanchez, S. I.; Bradley, S. A.; Li, A.; Szlufarska, I.; Voyles, P. M. *Nat. Commun.* **2014**, *5*, 4155.
(45) Bals, S.; Aert, S. V.; Tendeloo, G. V.; Ávila-Brande, D. *Phys. Rev. Lett.* **2006**, *96*, 096106.
(46) Kilaas, R. MacTempas: a program for Simulating high resolution TEM images and diffraction pattern. Total Resolution LLC, http://www.totalresolution (accessed on 06/09/2017).

DOI: 10.1021/acs.nanolett.7b03817
Nano Lett. 2018, 18, 717−724